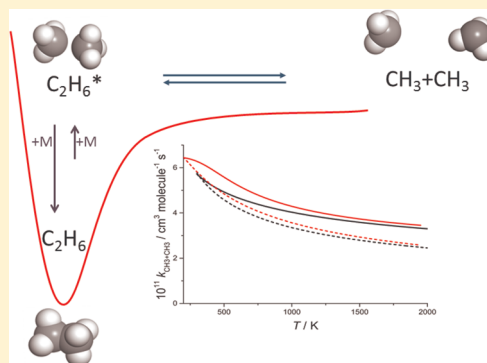


Reanalysis of Rate Data for the Reaction $\text{CH}_3 + \text{CH}_3 \rightarrow \text{C}_2\text{H}_6$ Using Revised Cross Sections and a Linearized Second-Order Master EquationM. A. Blitz,[†] N. J. B. Green,[‡] R. J. Shannon,[†] M. J. Pilling,^{*,†} P. W. Seakins,[†] C. M. Western,[§] and S. H. Robertson^{||}[†]School of Chemistry, University of Leeds, Leeds LS2 9JT, U.K.[‡]Inorganic Chemistry Laboratory, University of Oxford, South Parks Road, Oxford OX1 3QR, U.K.[§]School of Chemistry, Cantock's Close, Bristol BS8 1TS, U.K.^{||}Dassault Systèmes, BIOVIA, Science Park, Cambridge CB4 0WN, U.K.

Supporting Information

ABSTRACT: Rate coefficients for the $\text{CH}_3 + \text{CH}_3$ reaction, over the temperature range 300–900 K, have been corrected for errors in the absorption coefficients used in the original publication (Slagle et al., *J. Phys. Chem.* **1988**, 92, 2455–2462). These corrections necessitated the development of a detailed model of the $\tilde{\text{B}}^2\text{A}_1' (3\text{s}) - \tilde{\text{X}}^2\text{A}_2''$ transition in CH_3 and its validation against both low temperature and high temperature experimental absorption cross sections. A master equation (ME) model was developed, using a local linearization of the second-order decay, which allows the use of standard matrix diagonalization methods for the determination of the rate coefficients for $\text{CH}_3 + \text{CH}_3$. The ME model utilized inverse Laplace transformation to link the microcanonical rate constants for dissociation of C_2H_6 to the limiting high pressure rate coefficient for association, $k_\infty(T)$; it was used to fit the experimental rate coefficients using the Levenberg–Marquardt algorithm to minimize χ^2 calculated from the differences between experimental and calculated rate coefficients. Parameters for both $k_\infty(T)$ and for energy transfer $\langle \Delta E \rangle_{\text{down}}(T)$ were varied and optimized in the fitting procedure. A wide range of experimental data were fitted, covering the temperature range 300–2000 K. A high pressure limit of $k_\infty(T) = 5.76 \times 10^{-11} (T/298 \text{ K})^{-0.34} \text{ cm}^3 \text{ molecule}^{-1} \text{ s}^{-1}$ was obtained, which agrees well with the best available theoretical expression.



1. INTRODUCTION

The association of two methyl radicals



is important in combustion chemistry as a termination reaction and as a source of C₂ species in methane oxidation¹ and in planetary atmospheres following methane photolysis.^{2,3} The reaction has been widely studied experimentally, and Baulch et al.⁴ provide a critical analysis of the data, although they omit some more recent determinations.

The reaction is pressure dependent and is usually parametrized for combustion applications using the Troe approach,^{5,6} although the use of Chebyshev polynomials is increasing.⁷ The limiting high pressure rate coefficient, $k_\infty(T)$, is a key parameter but is more difficult to determine experimentally at higher temperatures, as the reaction moves increasingly into the falloff region as the temperature is increased at accessible pressures. Theoretical methods have improved considerably and high level calculation arguably provides a more accurate determination of $k_\infty(T)$ than does extrapolation of experimental data. The radial potential energy

is barrierless and variational methods, such as flexible transition state theory⁸ and the statistical adiabatic channel model,⁹ are required, making demands on the quality of both the radial and angular potentials. Klippenstein et al.¹⁰ demonstrated clearly the importance of the level of theory used to calculate the potential. They used a variety of approaches, finding CASPT2 provided the most accurate form for the potential energy, and concluded that methods that include dispersion interactions are essential. They showed that spin contamination effects become important at shorter bond distances, as the separation in the energies of the singlet and triplet surfaces, correlating with the two spin $1/2$ radicals, increases. They also incorporated dynamical effects of recrossing the dividing surface between (energized) C_2H_6 and the radicals, proposing an overall

Special Issue: 100 Years of Combustion Kinetics at Argonne: A Festschrift for Lawrence B. Harding, Joe V. Michael, and Albert F. Wagner

Received: January 30, 2015

Revised: May 7, 2015

Published: May 20, 2015



decrease in $k_{\infty}(T)$ of 15%. The analysis showed that the rate coefficient decreases with temperature, by a factor close to 2 over the range 300–2000 K. Earlier, Klippenstein and Harding¹¹ compared their MRCI calculations with a master equation (ME) analysis of the experimental data. They found that their calculated values exceeded those from the ME analysis of the rate data (in Ar), by a factor that increased with temperature, reaching a 3-fold difference at 1700 K.

The experimental data of Slagle et al.¹² have been most widely used in comparison between theory and experiment at temperatures up to 1000 K. The measurements were based on pulsed laser photolysis and two radical detection techniques, photoionization mass spectrometry (PIMS) at low bath gas densities $[(2-30) \times 10^{16} \text{ molecule cm}^{-3}]$ and absorption spectroscopy (AS) at higher densities (1.5×10^{17} to $1.5 \times 10^{19} \text{ molecule cm}^{-3}$). The AS measurements required the methyl radical absorption cross-section, σ , to convert the second-order radical absorbance decays into concentration profiles and hence rate coefficients. σ is temperature dependent and $\sigma(T)$ was measured by Macpherson et al.^{13,14} over the temperature range 296–537 K and compared to values calculated at temperatures up to 700 K. The rate coefficients were also measured, as a function of pressure, over the 296–577 K range. Subsequent measurements were made at temperatures up to ~ 900 K with the cross-section determined by a simple extrapolation of a power series representation of $\sigma(T)$, based on the lower temperature data, without the benefit of further calculations of the cross section at temperatures above 700 K.¹² These values were later criticized by Hessler and Ogren¹⁵ who compared the extrapolated cross sections with narrow line width laser measurements, finding significant differences.

In view of the importance of these AS measurements in providing an experimental set of pressure and temperature dependent rate coefficients that are relatively close to the high pressure limit, we report here revised cross sections, based on a new set of calculations that have been tested against the lower temperature experimental measurements and against higher temperature measurements of Oehlschlaeger et al.¹⁶ The revised cross sections are then used to correct the rate coefficients. The master equation code MESMER¹⁷ is then used to fit the experimental data, using inverse Laplace transformation of the high pressure limiting rate coefficient, $k_{\infty}(T) = A(T/298)^n$, to determine the microcanonical rate constants ($k(E)$) required for the ME calculation. The fitting was based on the optimization of the fitting parameters, A , n , and the parameters $\langle \Delta E \rangle_{\text{down,ref}}$ and m in an exponential down model of collisional energy transfer ($\langle \Delta E \rangle_{\text{down}} = \langle \Delta E \rangle_{\text{down,ref}}(T/298)^m$). The method thus provides a direct determination of $k_{\infty}(T)$, which is compared with the theoretical values of Klippenstein et al.,¹⁰ over the temperature range 300–900 K.

Although the AS measurements provide the set of rate data under conditions closest to the high pressure limit, there is an extensive set of data available covering a wide range of conditions. These data were also fitted using the MESMER methodology. This has allowed both the testing and reassessment of the high pressure limit over the temperature range 300–2000 K. In addition, the lower pressure data provide a more extensive means of determining the energy transfer parameters.

Section 2 reports the methods used for the redetermination of the absorption cross section for analysis of the AS data. Section 3 briefly outlines the master equation methodology.

This section also includes a discussion of the approach used to link the second-order rate coefficients to the high pressure rate coefficient and energy transfer parameters. This discussion is important because the master equation approach is usually based on a first-order analysis of the kinetics and an exponential representation of the radical decay, but for this reaction a second-order formulation is required, so the analysis is based on a local linearization, either within the experimental decay or as equilibrium is approached. Section 4.1 presents an analysis of the AS data and gives the best fit parametrizations for $k_{\infty}(T)$ and for $\langle \Delta E \rangle_{\text{down}}(\text{Ar})$. Section 4.2 extends the analysis to other measurements. The fits are done to all of the available experimental data and also with some degree of selectivity, which is rationalized in the Supporting Information. Section 5 compares the experimental fits with theory.

2. UV ABSORPTION CROSS SECTION OF THE $\tilde{\text{B}}^2\text{A}_1'$ ($3s$)– $\tilde{\text{X}}^2\text{A}_2''$ TRANSITION IN CH_3

The experimental kinetics resulting from absorption spectroscopy^{12,18,19} all use measurements at selected single wavelengths and rely on knowing the absorption cross section at these wavelengths under the experimental conditions, particularly the temperature dependence. Unfortunately, the B–X electronic transition used is far from ideal for this sort of work, as not only is the upper state strongly predissociated but also the pattern of vibrational and rotational levels is not fully known for either state. A further complicating factor is that the available spectroscopic information does not cover the full temperature range of the kinetic measurements. However, given the importance of the B–X transition in CH_3 , there has been some spectroscopy on this and related transitions that postdates some of the kinetics measurements, and it is worth reanalyzing these kinetic measurements in the light of these newer data. In addition, we can investigate the sensitivity of the cross sections, and hence the derived kinetic parameters, for a range of different assumptions about the missing data. In this section we present a selection of simulated absorption cross sections as a function of temperature under different assumptions.

2.1. Ground State CH_3 . The literature on the spectroscopy of the ground electronic state is reasonably comprehensive; the most recent relevant paper is by Kawaguchi,²⁰ containing a high resolution Fourier transform spectrum of the ν_3 band, the asymmetric stretch, which, combined with measurements of the same band by Amano et al.,²¹ gave a set of rotational constants for the zero-point level as well as the $\nu_3 = 1$ level. The symmetric stretch, ν_1 , is infrared inactive, but a rotationally resolved coherent Raman spectrum of the ν_1 fundamental has been reported by Triggs et al.²² with some overtones reported by Westre and co-workers.^{23,24} The out-of plane bending mode, ν_2 has a relatively low frequency (606 cm^{-1}) so excited bending levels must be included in the simulations, but fortunately high resolution diode laser spectra of the ν_2 fundamental and two hot bands have been reported by Yamada et al.,²⁵ and lower resolution spectra of higher levels are available from Hermann and Leone.²⁶ Surprisingly, given that the degenerate bending vibration, ν_4 , should be infrared active, the only available experimental measurements are in a matrix, complicated by the presence of rotational structure persisting in the matrix. The strongest component in matrix spectra is the $\text{R}_0(0)$ transition, expected about 14 cm^{-1} higher than the ν_4 band origin. Measurements in a neon matrix²⁷ and argon matrix²⁸ thus suggest a band origin of $1382-3 \text{ cm}^{-1}$, and measurements in a

para hydrogen matrix²⁹ suggest a band origin of 1387 cm⁻¹. A recent high level *ab initio* calculation by Cunha de Miranda et al.³⁰ predicted an anharmonic frequency of 1390 cm⁻¹ for ν_4 ; the same calculation predicted the other modes to within 4 cm⁻¹. In the absence of other information, we use a simple average of 1387 cm⁻¹ for ν_4 . Because the line width in the excited state is greater than 65 cm⁻¹, the uncertainty in the frequency of ν_4 is not significant.

Apart from ν_4 , all the lower rovibrational levels are thus well characterized. To make the best use of the available data, we refitted using the PGOPHER program³¹ to all the rotationally resolved data given above, which resulted in minor adjustments to the published constants. For details of this fit, and the final constants used see the Supporting Information. As the molecule is a symmetric top, only the changes to C , D_K , and H_K from the zero-point level are determined from the spectroscopy, so we fixed these at the values estimated by Kawaguchi²⁰ from planarity constraints. For ν_4 we took the band origin as 1387 cm⁻¹ and simply took the zero-point rotational constants, with the Coriolis coupling constant calculated from the sum rule $\zeta_3 + \zeta_4 = B/2C - 1$ given by Meal and Polo.³²

To complete the ground state calculation, the partition function is required. The vibrational partition function has been discussed by Medvedev et al.,³³ who demonstrated clearly that anharmonicity must be taken into account to obtain accurate partition functions at higher temperatures. On the basis of an explicit sum over levels calculated from a high quality *ab initio* surface, they showed the partition function calculated assuming harmonic levels was 1.5 times the true value at 2000 K, rising to a factor of 3 at 3000 K. The error arises mainly from the negative anharmonicity in ν_2 . Their calculated levels were, however, 10–20 cm⁻¹ in error compared to the observed values (where available), so our calculation was based on a fit to experimental levels. The band origins from the rotational calculation above were combined with some additional lower resolution data^{23,24,26} and fitted to the conventional power series expansion for vibrational levels in $(\nu + 1/2)$. These available data allowed the determination of the anharmonicity in ν_1 and ν_2 . The vibrational partition function was then calculated by an explicit sum over states. This gave values very similar to that from an explicit sum over states of the 64 levels given by Medvedev et al.,³³ with the discrepancy rising from 1% at temperatures around 1100 K, and this only because more than 64 levels were required to converge the sum. To investigate the effect of ignoring the anharmonicity in ν_4 , the energy level fit was extended to include the $2\nu_4$ and $3\nu_4$ from Medvedev et al.³³ This had a minor effect on the partition function (1% at 3000 K) so the error from ignoring the anharmonicity in the higher frequency ν_3 mode is probably negligible.

The complete partition function including rotation was then calculated on the basis of a simple sum, Q_{rovib} , over all rovibrational states for all states up to and including the $\nu_3 = 1$ level at 3160 cm⁻¹. This required adding $\nu_2 + \nu_4$, $2\nu_2 + \nu_4$, $2\nu_4$, and $4\nu_2$ levels to the rovibrational calculation, with estimated values of the constants. To correct for the vibrational levels excluded from this sum, two vibrational partition functions were calculated by an explicit sum over (only) vibrational levels, one with all vibrational levels (Q_{vib}), and the other a partial sum over the vibrational levels up to $\nu_3 = 1$, Q_{part} . The final partition function is then $Q_{\text{rovib}}/Q_{\text{part}} \times Q_{\text{vib}}$.

2.2. \tilde{B}^2A_1' Excited State. The excited state has long been known^{34,35} to show only poorly resolved vibrational structure, due to strong predissociation in the upper state, though the predissociation is sufficiently slower in CD₃ to show some rotational structure. Fortunately, an IR–UV double resonance study by Settersten et al.³⁶ was able to produce rotationally well resolved electronic spectra by preparing single rotational levels and were able to determine an accurate value for the band origin ($46\,239.4 \pm 1.2$ cm⁻¹). This origin is somewhat different from earlier experimental estimates of $46\,205$ ³⁴ and $46\,300 \pm 50$ cm⁻¹.³⁷ The imprecision results from the large width of the individual rotational levels; this was measured in detail for the origin band by Westre et al.³⁷ by rotational resonance Raman spectroscopy, who found widths of 65 cm⁻¹ for $J = 0$, increasing mildly with J . This was confirmed by Settersten et al.,³⁶ who also observed a moderate decrease in width with K , which was predicted, but not observed by Westre et al.³⁷ These widths limited the precision of the rotational constants but values of $B = 2C = 8.827$ cm⁻¹ from earlier work reproduced the observed spectra. Centrifugal distortion was ignored, as it would not have been measurable given the low resolution. The level dependence of the width is only poorly determined by the available data, so for this study a refit to the widths in Settersten et al.³⁶ and Westre et al.³⁷ was performed, giving the width as $w(J) = 82 + 0.08J(J + 1)$ cm⁻¹.

Given the temperature range, hot bands must also be considered, and the information on vibrationally excited states in the \tilde{B} state is limited. The absorption spectrum shows³⁵ two broad absorptions at shorter wavelengths than the origin band. The longer wavelength feature of these, at 47 015 cm⁻¹, was identified as a 0100–0100 hot band on the basis of temperature dependence; this was confirmed by a subsequent resonance Raman study.³⁸ This implies a significantly higher value for ν_2 in the excited state, which has been explained as due to pseudo-Jahn–Teller vibronic mixing with the ground state.²⁵ The line widths of this transition have only been measured for CD₃,³⁷ where it was found to be 2–3 times that of the origin level, depending on J' . In the absence of other information the widths of the origin level are simply multiplied by 2.5 for $\nu_2 = 1$, which gives a hot band spectrum with no structure reasonably consistent with that given by Callear and Metcalfe.³⁵

The shortest wavelength feature in the absorption spectrum, at 48 345 cm⁻¹ is very broad; resonance Raman spectroscopy has identified this as the 1000–0000 transition in the symmetric stretch, and measured the width at 400 cm⁻¹.³⁷ This corresponds to an excited state stretching frequency of 2100 cm⁻¹, significantly lower than the ground state value of 3160 cm⁻¹. This is consistent with the literature discussions of the predissociation mechanism, as dissociation to H + CH₂(\tilde{A}^1A_1) occurs with a low barrier, estimated to be 2200 cm⁻¹ from modeling the rotational dependence of the line widths,³⁷ and consistent with a high level *ab initio* calculation³⁹ that predicted a barrier of 2417 cm⁻¹. A low frequency anharmonic motion may thus be expected along the C–H stretching coordinate. The only available information on the degenerate modes ν_3 and ν_4 comes from an *ab initio* calculation by Mebel et al.,⁴⁰ predicting frequencies of 2794 and 1253 cm⁻¹. This work also calculated Franck–Condon factors, and predicted that the only vibrationally off-diagonal transitions with any significant intensity would have $\Delta\nu_1 = 1$, as for the 1000–0000 transition discussed above.

It is now possible to consider what hot bands need to be included for a complete simulation of the absorption in the

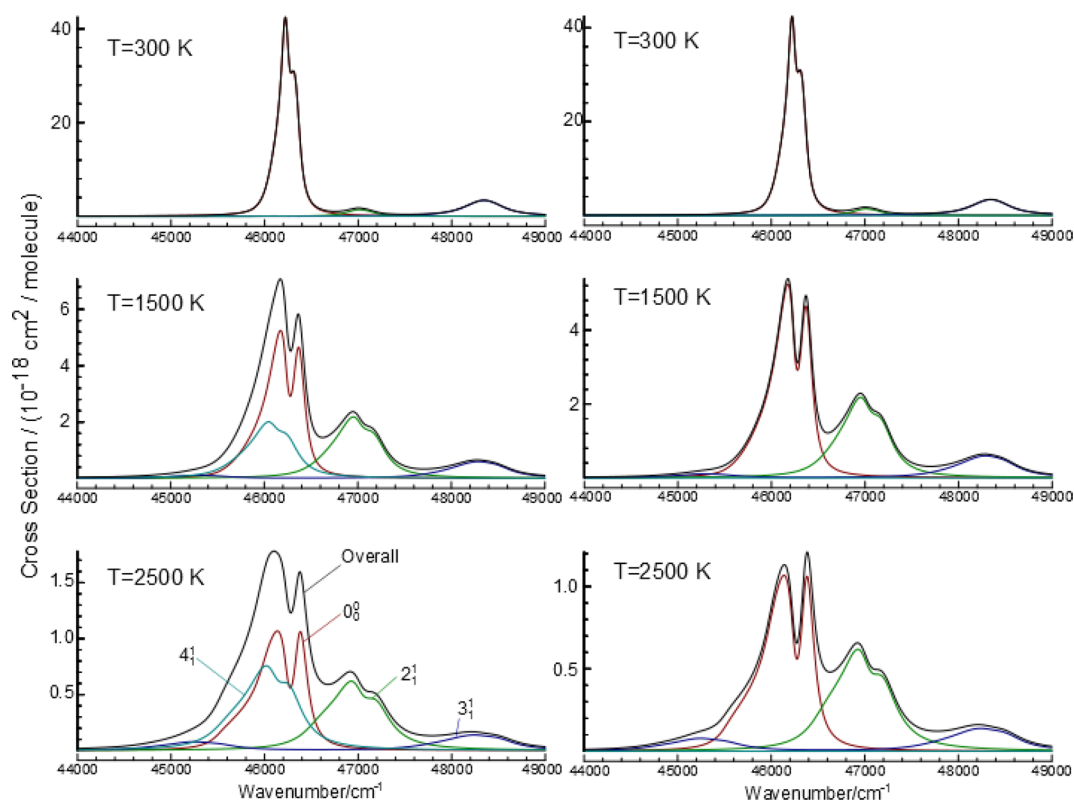


Figure 1. Simulated cross sections for the $\tilde{B}^2A_1' - \tilde{X}^2A_2''$ transition in CH_3 at various temperatures. The panels on the left are for model I described in the text, and those on the right are for model II, which excludes the ν_4 hot band. In each panel the top trace is the overall cross section, with the other traces giving the individual vibrational bands, as labeled in the bottom left panel. To agree with the low temperature experimental data, the cross sections need to be scaled up by 1.20.

region of the hot band at temperatures up to 2000 K. Hot bands involving the lowest frequency mode, ν_2 are likely to be significant, but the first, 0100–0100 is significantly shifted from the origin band because the bending frequency is significantly higher in the upper state, and bands involving higher ν_2'' , though significantly populated, will be at significantly higher frequency and will not contribute to the region of interest. As discussed above, the symmetric stretch is at a significantly lower frequency than the ground state, so the 1000–1000 hot band should be 1000 cm^{-1} below the origin, so again should not contribute. The same argument might be expected to apply to the degenerate stretch, ν_3 ; the low barrier to dissociation along the C–H stretching coordinate suggests the *ab initio* estimate of 2794 cm^{-1} for this is likely to be too high, and it is likely to be close to the symmetric stretch, giving a similar shift from the origin. In addition, the vibrational energy means that any absorption is likely to be broad and thus make a small contribution.

This leaves hot bands involving the degenerate bending motion, ν_4 , for which little experimental information is available, and the 0001–0001 band is likely to make a significant contribution to absorption at the wavelength of interest at the higher temperatures, given there is no indication of a large change in frequencies between the two states. The vibrational energy is similar to the 0100 level, so a similar width might be expected, but it is difficult to make further predictions. In the work here we will therefore use calculations with and without the 0001–0001 band as an indication of the uncertainty in the calculations, and assume the width is the same as $\nu_2' = 1$. In principle the 0002–0002 band might also contribute at the higher temperatures, but this is likely to be

above the barrier to dissociation, and thus too broad to give a significant contribution. This, and other hot band absorptions, could lead to a significant nonresonant background at higher temperatures given the number of possible populated states; at 2000 K only 10% of the population is in the ground vibrational state.

The final component needed is the strengths of the various bands. As a starting point, we use the oscillator strength of the origin band determined by Callear and Metcalfe³⁵ of $f = 0.0137 \pm 0.0015$. Setting up the rovibrational simulation in PGOPHER gave a spectrum with a profile in good agreement with a published spectrum at 293 K (compare the top left panel of Figure 1 with Figure 5 of Settersten et al.³⁶) For these calculations, model I included five vibrational bands: the origin band, 0100–0100, 1000–0000, 1000–1000, and 0001–0001. Model II excluded the ν_4 hot band, 0001–0001. To check the absolute absorption cross section, we make use of two measurements of the cross section at specific wavelengths. The first of these, by Macpherson et al.,¹³ measured the absorption at 216.36 nm in the range 296–537 K with a 0.6 nm triangular band-pass with an uncertainty of the individual measurements of about 5%. The second of these, by Oehlschlaeger et al.,¹⁶ measured the absorption at 216.62 nm over the higher temperature range 1200–2500 K, again with an estimated uncertainty in the absorption coefficient of 5%. The latter measurements were made with a very narrow bandwidth laser. To allow for a direct comparison of the two measurements, a correction factor for the lower temperature data is calculated by integrating the simulated spectra over a triangular function with 0.6 nm full width half-maximum, to match the function specified by Macpherson et al.,¹³ and comparing it to

the simulation at the spot wavelength of 216.62 nm. The correction is done to the low temperature data; as the discussion below will show, it is much less sensitive to the assumptions made in the simulation. This reduced the effective low temperature cross section by a factor of 0.80 at 300 K, increasing to 0.97 at 537 K as the spectrum broadened with temperature.

Table 1 shows calculated and observed values.

Table 1. Low Temperature Calculated and Observed Cross Sections at 216.62 nm for the $\tilde{B}^2A_1' - \tilde{X}^2A_2''$ Transition in CH_3

T/K	cross section ($10^{-17} \text{ cm}^2 \text{ molecule}^{-1}$)			
	calcd model I	calcd model II	obsd	corrected observn
298	2.67	2.67	4.05	3.23
301	2.67	2.67	4.12	3.29
350	2.62	2.61	3.92	3.28
405	2.55	2.52	3.46	3.04
472	2.44	2.39	3.16	2.92
537	2.32	2.25	2.67	2.58

At these relatively low temperatures, excluding or including ν_4 makes relatively little difference to the simulation, as shown in the similarities of models I and II (columns 2 and 3 of Table 1). The agreement between observed and either set of calculated values is quite good if the calculated values are scaled up by a factor of 1.20. As discussed above, the calculated values use the oscillator strength from Callear and Metcalfe³⁵ as a base for the intensity, so a correction factor of 1.2 is reasonable given the 11% error bars from that work³⁵ and the 5% error bars in Macpherson et al.¹³ This correction factor is used in the simulations described as scaled below.

Using the same parameters to simulate the high temperature data of Oehlschlaeger et al.¹⁶ reveals a significant discrepancy, in that the calculated values are all much too low, as can be seen in Table 2. The reason for this becomes apparent on looking at the absorption spectra published in that work, and in an earlier

Table 2. High Temperature Calculated and Observed Cross Sections ($10^{-18} \text{ cm}^2 \text{ molecule}^{-1}$) at 216.62 nm for the $\tilde{B}^2A_1' - \tilde{X}^2A_2''$ Transition in CH_3 ^a

T/K	cross sections ($10^{-18} \text{ cm}^2 \text{ molecule}^{-1}$)				
	model I	model II	model I + vib backgd	model II + vib backgd	Oehlschlaeger ¹⁶
1200	12.98	10.56	14.02	12.74	11.33
1300	11.28	8.96	12.50	11.30	9.89
1400	9.79	7.59	11.15	10.06	8.81
1500	8.47	6.43	9.98	8.99	7.96
1600	7.32	5.45	8.96	8.08	7.29
1700	6.33	4.62	8.07	7.30	6.75
1800	5.48	3.92	7.31	6.63	6.29
1900	4.74	3.34	6.65	6.06	5.92
2000	4.11	2.84	6.08	5.56	5.60
2100	3.57	2.43	5.59	5.14	5.32
2200	3.10	2.08	5.16	4.78	5.08
2300	2.71	1.79	4.79	4.46	4.87
2400	2.37	1.55	4.47	4.19	4.69
2500	2.08	1.34	4.19	3.95	4.53

^aThe calculated values include a scale factor of 1.20 to match the low temperature data.

paper from the same group.⁴¹ Although the simulation of the profile of the origin band is reasonable, it is clear that there is a significant very broad absorption that is not from the origin band, and this absorption is included in the cross section. At 1600 K this accounts for at least 50% of the absorption at the center of the origin band and is too large to be accounted for by an adjustment in the ν_4 hot band. In addition, the calculated cross section decreases much more rapidly with increasing temperature than the measured cross section. The implication is that there are a significant number of hot bands contributing to the spectrum at higher temperatures. As discussed above, there is no detailed information about these, but we expect them all to be broad as most, if not all of them, would be above the barrier to dissociation of the excited state at 2200 cm^{-1} . We therefore constructed an approximate model for this vibrational background using the following assumptions. The model included only vibrational levels, using the energy level pattern calculated from the constants determined as above. To determine the intensities, Franck–Condon factors were calculated assuming harmonic oscillator wave functions, with the displacement along the only symmetrical normal mode, ν_1 adjusted to match the relative Franck–Condon factors for the origin and 1000–0000 bands calculated by Mebel et al.⁴⁰ (The resulting set of Franck–Condon factors were similar, but not identical to those in Mebel et al.⁴⁰) The predissociation was accounted for by giving a width of 1000 cm^{-1} to all the transitions; the simulation is not very sensitive to the value chosen, and 1000 cm^{-1} gives a reasonable match to the long wavelength end of the spectrum given by Davidson et al.⁴¹ The overall cross section at 216.62 nm is then calculated by adding the cross section from the rovibronic simulation described above to the cross section from the background model. Any vibrational transitions included in the rovibrational model were excluded from the vibrational model. Figure 2 shows an overall simulation at 1600 K showing the effect of this vibrational background. Table 2 and Figure 3 present the temperature dependence of the cross section using the two models above with the vibrational background added. Note that both include the scaling factor of 1.2 to make the low temperature calculations match with the experiment.

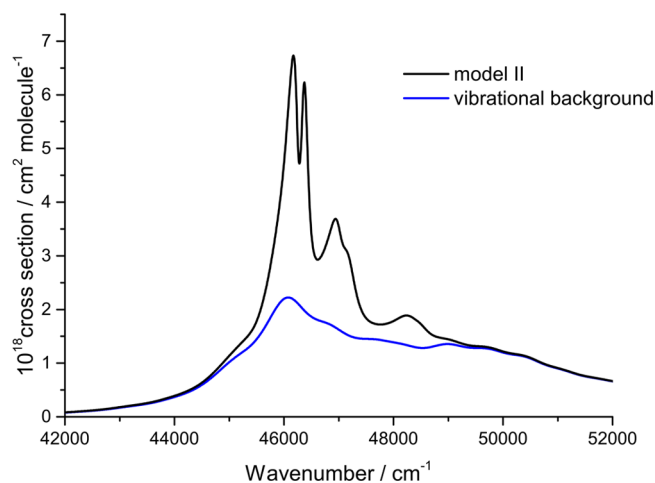


Figure 2. Simulated cross section for the $\tilde{B}^2A_1' - \tilde{X}^2A_2''$ transition in CH_3 at 1600 K. This is model II as described in the text, with the vibrational background model added. To agree with the low temperature experimental data, the cross sections need to be scaled up by 1.20.

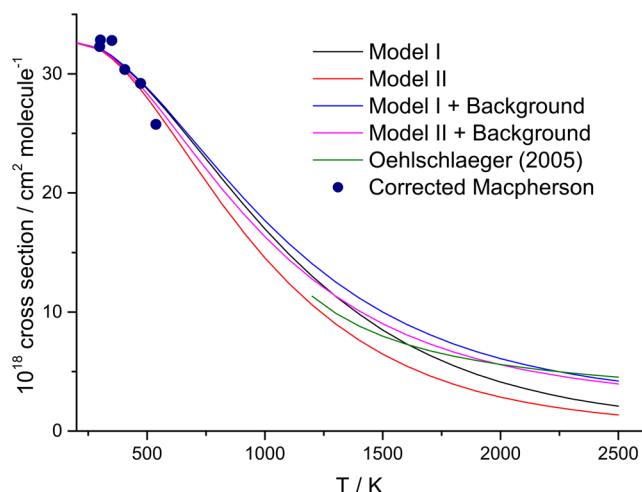


Figure 3. Cross section at 216.62 nm for the $\tilde{B}^2A_1' - \tilde{X}^2A_2''$ transition in CH_3 as a function of temperature. See text for a description of the various models, which include a scaling factor of 1.2 to make the calculated curves match the low temperature experimental data of Macpherson et al.¹³

All the models give good fits to the low temperature data, in part because we have used that to determine the absolute band strength. It is clear that models excluding the broad background give too low an absorption at high temperatures, and the best fit is model II + background, which includes the ν_4 hot band as part of the background, rather than in the rovibrational model, suggesting a width for this band rather larger than 200 cm^{-1} . This best fit model gives good agreement over a wide temperature range; an indication of the quality is obtained if the overall scaling factor is determined from the high temperature data, which gives a value of 1.18 in comparison with a factor of 1.20 from the low temperature data. This is probably as good as can be done with the available information as there are two obvious areas where information is lacking. One of these is the detailed rotational model for the origin band of the electronic transition. We only have limited rotational information, and so ignore centrifugal distortion completely and we only have a rough model for the rotational dependence of the line widths; both of these deficiencies are likely to lead to significant changes at high temperature. The vibrational background model is also obviously very approximate, though this is alleviated by the very low resolution required.

A set of models for the absorption cross section has been developed in this section and tested against low^{13,35} and high temperature¹⁶ experimental data. It was not possible to constrain the model fully using those data. In particular, it is not clear what contribution the ν_4 hot band makes to the absorption, leading to proposals of two models, one with (model I) and one without (model II) its full potential contribution. In addition, at higher temperatures, it is necessary to invoke a vibrational background contribution to reproduce experiment. The best representation is found with model II + vibrational background and it provides a means of calculating the absorption cross section at temperatures up to 2500 K with reasonable accuracy, using PGOPHER with the input data given in the Supporting Information. For the present application, we require cross sections up to 906 K, to refine the rate coefficients obtained by Slagle et al.¹² using absorption spectroscopy. The vibrational background makes little con-

tribution at these temperatures and models I and II adequately bracket the values needed to effect this refinement.

3. MASTER EQUATION METHODOLOGY

The application of the master equation to reactions in the gas phase has been extensively discussed elsewhere.^{17,42–45} Here, the main points are summarized and the manipulations required to accommodate second-order systems are discussed. Typically, the energy spaces of the species involved in a reaction are partitioned into a number of contiguous intervals or grains that are assigned values for the numbers of states they contain, average energies, and where appropriate, average values of microcanonical rate coefficients. These grains form the basis of the master equation representation of the system, an equation of motion of the grain probabilities, which is usually represented as

$$\frac{d\mathbf{p}}{dt} = \mathbf{M}\mathbf{p} \quad (1)$$

where \mathbf{p} is a vector containing the probability densities of the grains and the matrix \mathbf{M} contains the transition rates between the grains either because of collisional activation/deactivation or because of reaction. The evolution of \mathbf{p} is limited by two constraints, mass (or density) conservation and detailed balance.

The solution to eq 1 can in general be written as

$$\mathbf{p} = \mathbf{U}e^{\Lambda t}\mathbf{U}^{-1}\mathbf{p}_0 \quad (2)$$

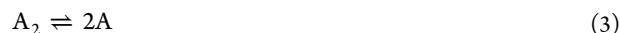
where Λ is a diagonal matrix containing the eigenvalues of \mathbf{M} , \mathbf{U} is a matrix of the corresponding eigenvectors, and \mathbf{p}_0 is a vector containing the initial grain densities. Though the detailed trajectories are often of interest, it is the effective macroscopic rate coefficients that are usually of greater concern for comparison with experiment or for use in reaction simulation schemes. The extraction of effective macroscopic rate coefficients can be achieved in a number of ways, but possibly the most easily automated way is the Bartsis–Widom algorithm, which is very effective in those cases where there is a clear separation of chemically significant eigenvalues (CSEs) from the rest of the eigenvalue spectrum.

The general form of the master equation given by eq 1 is applicable to systems in which reactions are first order, i.e., dissociation and isomerization, or are between two species, one of which is in excess; i.e., the reaction is pseudo first order. For such a system, eq 1 remains linear and the elements of \mathbf{M} remain independent of time. However, this is not the case for the title reaction, which is second order in a single species and so cannot be linearized by simply letting one of the reactants remain at its initial concentration.

This problem has been addressed by a number of workers. Possibly the simplest approach is to try to account for the temperature and pressure dependence of the association reaction by considering the rate coefficient for the irreversible unimolecular dissociation reaction and deriving the corresponding value for the association reaction by applying the equilibrium constant. Robertson et al.⁴⁶ applied this procedure in their analysis of the Slagle et al.¹² data for $\text{CH}_3 + \text{CH}_3$. The difficulty with this approach, apart from the numerical precision issues that were encountered (and circumvented by effectively assuming a reservoir state), is that it does not account for the possible effects of back-reaction, which can be significant in more complex reactions. Recently, Georgievskii et al.⁴⁷ have

reported a method in which they decouple the association reaction from the unimolecular species which offers another possible approach to the problem. Earlier, Davis and Klippenstein⁴⁸ reported a comprehensive analysis of the second-order association system and applied it to the title reaction. They examined models of the second-order association systems of increasing complexity, starting with a simple concentration model, until they reached a master equation representation of the system. The analysis that is applied here is closely related to that work.

Before looking at the full master equation analysis, it is perhaps best to re-examine the first simple model used by Davis and Klippenstein. For the second-order reaction,



The phenomenological rate expression for the forward reaction is

$$\frac{d[A_2]}{dt} = -k_f[A_2] + k_r[A]^2 \quad (4)$$

and at equilibrium the left hand side equals 0, giving

$$\frac{[A]_e^2}{[A_2]_e} = \frac{k_f}{k_r} = K_e \quad (5)$$

where k_f and k_r are the dissociation and association rate coefficients, respectively. Equation 4 has the form of the general kinetic equation of motion:

$$\frac{dc}{dt} = f(c) \quad (6)$$

where c is a vector of concentrations and $f(c)$ is a vector of functions such that the element $f_i(c)$ determines the evolution of concentration c_i , and there is an equilibrium concentration vector c_e such that

$$\frac{dc_e}{dt} = f(c_e) = 0 \quad (7)$$

A Taylor expansion of $f(c)$ about some arbitrary fixed point c_a gives

$$\frac{dc}{dt} = f(c_a) + \left(\frac{\partial f}{\partial c} \right)_{c_a} (c - c_a) + \dots \quad (8)$$

where $(\partial f / \partial c)_{c_a}$ is the Jacobian matrix containing all the partial derivatives $(\partial f_i / \partial c_j)_{c_a}$. Defining $\delta c = (c - c_a)$, it follows that

$$\frac{d\delta c}{dt} = \frac{dc}{dt} = f(c_a) + \left(\frac{\partial f}{\partial c} \right)_{c_a} \delta c \quad (9)$$

This equation shows that the evolution of the trajectory $c(t)$ in the neighborhood of c_a is governed by the Jacobian $(\partial f / \partial c)_{c_a}$ and the time constants will be the eigenvalues of the Jacobian. In the same way, as shown by Davis and Klippenstein, the time constants depend on time through their dependence on the concentration c_a . In the case considered, this dependence is simple and permits the identification of first and second-order rate coefficients for the dissociation and association steps, which do not depend on time, as shown by Davis and Klippenstein.⁴⁸

For reaction given by eq 3 the complete set of rate equations can be expressed as

$$\frac{d}{dt} \begin{pmatrix} [A_2] \\ [A] \end{pmatrix} = \begin{pmatrix} -k_f[A_2] + k_r[A]^2 \\ 2k_f[A_2] - 2k_r[A]^2 \end{pmatrix} = f([A], [A_2]) \quad (10)$$

Note that the form of eq 10 is such that it conserves mass. Constructing the equivalent of eq 9,

$$\frac{d}{dt} \begin{pmatrix} \delta[A_2] \\ \delta[A] \end{pmatrix} = f'([A]_a, [A_2]_a) + \begin{pmatrix} -k_f & 2k_r[A]_a \\ 2k_f & -4k_r[A]_a \end{pmatrix} \begin{pmatrix} \delta[A_2] \\ \delta[A] \end{pmatrix} \quad (11)$$

Note that the Jacobian in eq 11 now depends on the rate coefficients k_f and k_r as well as the local concentration of A at the point of expansion. The eigenvalues of the above matrix are 0 and $-(k_f + 4k_r[A]_a)$. The zero eigenvalue follows from mass conservation. The other eigenvalue governs the rate of motion along the trajectory in the region of the concentration $[A]_a$. If the eigenvalue is known, then, together with the equilibrium constant expression (eq 5), the effective macroscopic rate coefficients, k_f and k_r , can be obtained.

The above description does not, of course, account for pressure effects, and to do this the model must be extended to include regular gas kinetic master equation terms. The development follows along similar lines, the nonlinear master equation being

$$\frac{dp}{dt} = \begin{pmatrix} [\omega(P - \mathbf{1}) - K_f]p' + k_r\varphi[A]^2 \\ 2k_f \cdot p' - 2k_r[A]^2 \end{pmatrix} \quad (12)$$

where $p = (p', [A])$, and results in a Jacobian matrix of the form

$$J = \begin{pmatrix} \omega(P - \mathbf{1}) - K_f & 2k_r\varphi[A]_a \\ 2k_f & -4k_r[A]_a \end{pmatrix} \quad (13)$$

where K_f is a diagonal matrix whose elements are the same as the vector k_f (the microcanonical dissociation rate coefficient), k_r is the association rate coefficient, φ is the distribution function of the energy of the associated product formed in the reaction (i.e., the chemical activation distribution) and is obtained from k_f by detailed balance, P is the matrix of collisional transition probabilities, $\mathbf{1}$ is the identity matrix, and ω is the collision frequency. The Jacobian in eq 12 appears to differ from that obtained by Davis and Klippenstein.⁴⁸ This is because they accounted for mass conservation explicitly by eliminating a differential equation and replacing it with the mass conservation equation, whereas in the above mass conservation is implicit in the Jacobian and results in the zero eigenvalue. This form, rather than the Davis and Klippenstein form was employed, as it was easier to implement alongside other reaction models within the MESMER framework. The effective rate coefficients follow from the leading nonzero eigenvalue and the equilibrium constant. In a more complex scheme with simultaneous isomerization the Bartis–Widom⁴⁹ analysis of J might resolve the additional complications, but this requires further analysis and is currently under investigation.

4. ANALYSIS OF THE ABSORPTION SPECTROSCOPY DATA

4.1. Fits to Modified Absorption Spectroscopy Data.

The experimental data from Slagle et al.,¹² based on absorption spectroscopy, were modified using the absorption coefficients discussed in section 2. The experiment directly returned values

for k/σ where σ is the coefficient for the experimental bandwidth of 0.6 nm. The corrections were scaled to a value of unity at 300 K in applying the correction, because this was the temperature at which Macpherson et al.¹³ made the most detailed measurements. The resulting correction factors and the rate coefficients are given in Table S1 in the Supporting Information. The modified cross sections from models I and II were used and provide appropriate upper and lower bounds for the cross section (Figure 3). The vibrational background has a negligible effect over the experimental range (296–906 K).

As discussed above, the microcanonical rate constants for dissociation of C_2H_6 , for incorporation in the master equation, were determined by inverse Laplace transformation (ILT) of the high pressure rate coefficient for association, $k_\infty(T)$.⁵⁰ This procedure provides a direct link, through the master equation, between the pressure and temperature dependent experimental rate coefficients and one of the main targets of the analysis, $k_\infty(T)$. The master equation was used to calculate $k(p,T)$ for each of the 102 experimental conditions using A , n , $\langle\Delta E\rangle_{\text{down,ref}}$ and m as variable parameters. The differences between experimental and calculated values of $k(p,T)$ were minimized, with χ^2 as the criterion of best fit using the Levenberg–Marquardt algorithm, to obtain the best-fit parameters A , n , $\langle\Delta E\rangle_{\text{down,ref}}$ and m . This procedure is available within the MESMER code.^{17,51}

The value of χ^2 per degree of freedom for the fit is 0.44; the experimental values for the measured uncertainty in k were employed in weighting, suggesting that these uncertainties are possibly overestimated or contain a systematic component. The best fit parameters are shown in Table 3. Figure 4 shows a plot of the experimental values of $k(p,T)$ vs the calculated values, based on model I for the absorption cross section. A linear fit, forced through the origin, is shown. The slope is 0.992 and $R^2 = 0.979$.

An equally good fit was obtained using model II for the cross section. As shown in Table 3, this fit gives a slightly stronger negative temperature dependence, but with $k_\infty(900\text{ K})$ differing by only 9% from that returned by model I. The estimates of the energy transfer parameters, however, differ substantially between the fits obtained using the two absorption coefficient models. The differences in the rate coefficients between the two models are only modest, and this result demonstrates the comparative insensitivity of the data to energy transfer: the measurements are too close to the high pressure limit, even at high temperature, to provide a precise representation of $\langle\Delta E\rangle_{\text{down}}(T)$.

4.2. Extended Analysis. There have been several measurements of $k(p,T)$ over a range of conditions (Table 4), and many of these studies have been included in an extended set of fits using the MESMER code; each of these fits has included the modified experimental data discussed in section 4.1. The results of three of these fits are presented in Table 3; further examples are presented in the Supporting Information.

In addition to the absorption spectroscopy data from fit 1, fit 4 is primarily based on measurements at low temperatures ($\leq 700\text{ K}$) and low pressures, in He and Ar, made using pulsed photolysis and photoionization mass spectrometry. The most extensive set of data in this category derives from Slagle et al.,¹² in a joint paper with the absorption spectroscopy measurements discussed above. In addition, higher pressure data were obtained by Pereira et al.⁵³ using absorption spectroscopy at temperatures up to 700 K. The measurements were secondary to a determination of the rate coefficient for $CH_3 + OH$ and the

Table 3. Best Fit Parameters from Master Equation Fits^a

data set, cross section model ^b	A^c	n	$\langle\Delta E\rangle_{\text{down,ref}}^d$ Ar	m Ar	$\langle\Delta E\rangle_{\text{down,ref}}^d$ He	m He	$B(\text{Ar})^e$	no. of data points	$\chi^2/\text{degree of freedom}$	temp range/K
1. Slagle et al., ¹² PPAS, model I	5.66 (0.09)	−0.25 (0.04)	263 (33)	0.676 (0.16)				102	0.44	296–906
2. Slagle et al., ¹² PPAS, model II	5.68 (0.09)	−0.334 (0.04)	326 (33)	0.17 (0.14)				102	0.46	296–906
3. Slagle et al., ¹² PPAS, original	5.79 (0.10)	−0.423 (0.04)	171 (21)	1.14 (0.17)				102	0.61	296–906
4. refs 12 and 52–55, model I	5.63 (0.08)	−0.23 (0.04)	278 (27)	0.626 (0.10)	111 (16)	1.46 (0.17)		185	0.70	296–1350
5. data from fit 4 plus Oehlschlaeger et al., ¹⁹ model I	5.73 (0.08)	−0.26 (0.03)	302 (21)	1.57 (0.29)	102 (14)	1.56 (0.16)	1.24×10^{-3}	(0.30 × 10 ^{−3})	212	0.59
6. data from fit 4 plus Oehlschlaeger et al., ¹⁹ model II	5.79 (0.09)	−0.41 (0.03)	287 (20)	1.29 (0.29)	93 (12)	1.73 (0.16)	0.89×10^{-3} (0.29 × 10 ^{−3})	212	0.88	296–1924

^aThe quantities in brackets are the 1 σ uncertainties, as returned from the Levenberg–Marquardt fits. ^bTechnique: PPAS: pulsed photolysis, absorption spectroscopy. ^c10^{−11} cm³ molecule^{−1} s^{−1}. ^dK^{−1}.

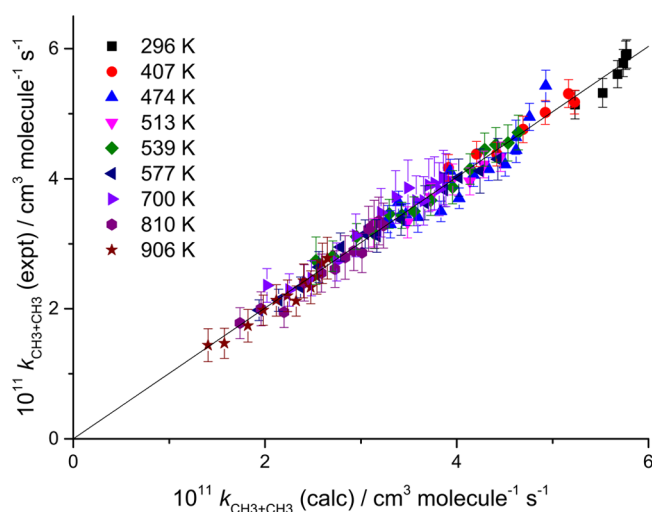


Figure 4. Plot of the experimental rate coefficients,¹² corrected using model I for the absorption cross section, vs the best fit values from the master equation fit.

technique was not optimized for absorption spectroscopy. These data required correction for the absorption cross section, and model I was used in fit 4. Even higher pressure measurements were made by Hippler et al.⁵² at 296 K. Finally, a limited set of measurements was made at 1350 K by Glänzer et al.⁵⁵ using a shock tube with absorption spectroscopy. Fit 4 returns very similar ILT parameters to fit 1 and the energy transfer parameters for Ar are comparable. The fit also returns energy transfer parameters for He, using a facility in the MESMER code that allows fitting to different bath gases, with different energy transfer parameters, but constrained to the same ILT parameters and hence to the same microcanonical rate constants for dissociation of $C_2H_6^*$.

The temperature range was considerably extended in fit 5 by including the shock tube data of Oehlschlaeger et al.¹⁹ They measured the dissociation of C_2H_6 in Ar, by monitoring the initial rise of $[CH_3]$ at low concentrations of ethane, to avoid interfering reactions. The absolute values of $[CH_3]$ were determined by absorption spectroscopy; the absorption cross sections were measured directly¹⁶ and the results form the basis of the high temperature models developed in section 2. The dissociation rate coefficients were converted into association rate coefficients using the equilibrium constant calculated from the thermochemical database of Goos et al.⁵⁷ The fits were poor with the usual representation of the temperature dependence of $\langle \Delta E \rangle_{\text{down}}$. It was necessary to apply a different set of energy transfer parameters to these shock tube data,

significantly reducing the increase in $\langle \Delta E \rangle_{\text{down}}$ with T (Supporting Information). An alternative approach was taken in fit 5 using a three parameter expression for Ar: $\langle \Delta E \rangle_{\text{down}} = \langle \Delta E \rangle_{\text{down,ref}} (T/298)^m \exp(-BT)$ and the best fit parameters are shown in Table 3. This representation should be interpreted simply as a heuristic approach to fitting the data, with no intrinsic theoretical justification. It is suggested in section 5 that this observation may be associated with the recent demonstration of the importance of collisional angular momentum relaxation, as well as total energy relaxation, in association reactions.⁵⁸ The angular momentum distributions in the reaction system will differ considerably at low and at high temperatures.

The ILT parameters A and n are changed relatively little in the extended fit; the two expressions for k_∞ from fits 4 and 5 differ by only 2% across the temperature range. Figure 5 shows

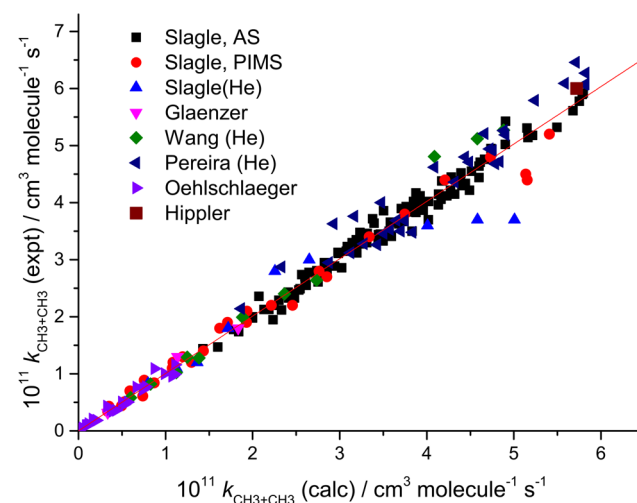


Figure 5. Plot of the experimental rate coefficients vs the best fit values from the master equation fit 5. The data refer to Slagle et al.,¹² Glänzer et al.,⁵⁵ Wang et al.,⁵⁴ Pereira et al.,⁵³ Oehlschlaeger et al.,¹⁹ Hippler et al.⁵²

a plot of the calculated values of $k(p,T)$ vs the experimental values from fit 5 and identifies the sources of the rate data. Although the scatter is somewhat larger than is the case for Figure 4, it is still very satisfactory given the range of sources of the data, the extended temperature range and the wide range in magnitude of the rate coefficients. The slope is 0.993 and $R^2 = 0.979$. The Supporting Information includes a representation of $k(p,T)$ for the Ar data from this fit using Chebyshev polynomials.

Table 4. Measurements of the Rate Coefficient for $CH_3 + CH_3$ Included in the Master Equation Fits Discussed in Section 4

technique ^a	temp range/K	bath gas (M)	$[M]/\text{molecule cm}^{-3}$	reference
PP/AS	296–906	Ar	8.6×10^{16} to 1.6×10^{19}	Slagle et al. ¹²
PP/PIMS	296–906	Ar, He	1.8×10^{16} to 3.4×10^{17}	Slagle et al. ¹²
PP/AS	296	Ar	2.5×10^{19} to 5×10^{21}	Hippler et al. ⁵²
PP/AS	290–700	He	1.6×10^{17} to 2.2×10^{19}	Pereira et al. ⁵³
PP/PIMS	305–715	He	2.2×10^{16} to 3.2×10^{17}	Wang et al. ⁵⁴
ST/AS	1350 K	Ar	1.2×10^{18} to 1.2×10^{20}	Glänzer et al. ⁵⁵
ST/AS	1175–1750	Ar	5.4×10^{18} to 1.1×10^{19}	Du et al. ¹⁸
ST/AS	1343–2034	Ar	4.6×10^{17} to 3.9×10^{19}	Oehlschlaeger et al. ¹⁹
ST/Schlieren	630–2200	Kr	2.8×10^{17} to 1.8×10^{18}	Yang et al. ⁵⁶

^aTechniques: PP, pulsed photolysis; AS, absorption spectroscopy; PIMS, photoionization mass spectrometry; ST, shock tube.

Fit 6 shows the effects of using the low temperature absorption spectroscopy data corrected using model II for the absorption spectroscopy data from Slagle et al.¹² Note that in both fits 5 and 6 the data from Oehlschlaeger et al.¹⁹ were used directly without any correction to the cross sections, which were directly measured across the whole temperature range. Indeed, these absorption data were used to assess the different absorption cross section models in section 2.

Two other sets of rate data were used; they are shown in Table 4 and are discussed in greater detail in the Supporting Information. Du et al.¹⁸ used azomethane dissociation to generate CH₃ with Ar as a bath gas but obtained values ~70% lower than those of Oehlschlaeger et al.,¹⁹ with greater scatter. The measurements of Yang et al.⁵⁶ involved dissociation of CH₃I and were made in Kr at lower pressures (20–280 Torr). They are more scattered than the data shown in Figure 5, and the low pressures mean that these data did not constrain *A* and *n* significantly. They do, though, provide estimates of the energy transfer parameters for Kr over a wide experimental range. Values are reported in the Supporting Information; the paper reports dissociation rate coefficients, which were converted into association rate coefficients using Goos et al.⁵⁷

4.3. Uncertainties. A primary goal of this paper is the determination of $k_{\infty}(T)$ for the CH₃ + CH₃ reaction and its comparison with the best theoretical determinations. An assessment of the overall uncertainty in the limiting rate coefficients, resulting from the scatter in the experimental measurements and the fitting process, is essential in such a comparison. Table 5 gives the correlation matrix for fit 5 and

Table 5. Correlation Matrix for Fit 5

$\langle \Delta E_{\text{down}} \rangle$	<i>m</i>	<i>B</i>	<i>A</i>	<i>n</i>
1				
−0.511	1			
0.3799	0.58933	1		
−0.98676	-5.23×10^{-1}	−0.4117	1	
−0.6337	0.14495	0.392505	−0.6954	1

demonstrates the strong correlations between all the fitted parameters. It is essential that these correlations are properly incorporated into the determination of the confidence limits for $k_{\infty}(T)$, which were obtained in the following manner. The methodology, in a similar context, is discussed in more detail in a recent publication.⁵⁹

First, joint probability distributions, accounting for correlations between all parameters, were obtained as described in Kucherenko et al.⁶⁰ An inverse cumulative distribution function was used to transform a Sobol sequence, consisting of 1000 elements, into a set of standard normal sample vectors $\{\tilde{\mathbf{x}}\}$. A Cholesky decomposition, *A*, of the covariance matrix, *Σ*, from the Marquardt fitting was then calculated:

$$\Sigma = \mathbf{A}\mathbf{A}^T \quad (14)$$

and a set of joint probability distributions of the parameters $\{\mathbf{x}\}$ was obtained from $\tilde{\mathbf{x}}$ as follows:

$$\mathbf{x} = \mathbf{A}\tilde{\mathbf{x}} + \boldsymbol{\mu} \quad (15)$$

Here $\boldsymbol{\mu}$ is a vector of the mean values for each parameter as taken from the best fit values from the Marquardt fitting procedure. Calculations of the CH₃ + CH₃ association rate coefficient were then performed using MESMER at temperatures between 300 and 2000 K at limiting high pressures, the

value of the fitted parameters in each calculation being taken sequentially from $\{\mathbf{x}\}$. Finally, confidence limits were taken from 2σ values for the distribution at each temperature. These limits are shown in Figure 6, which is discussed in more detail

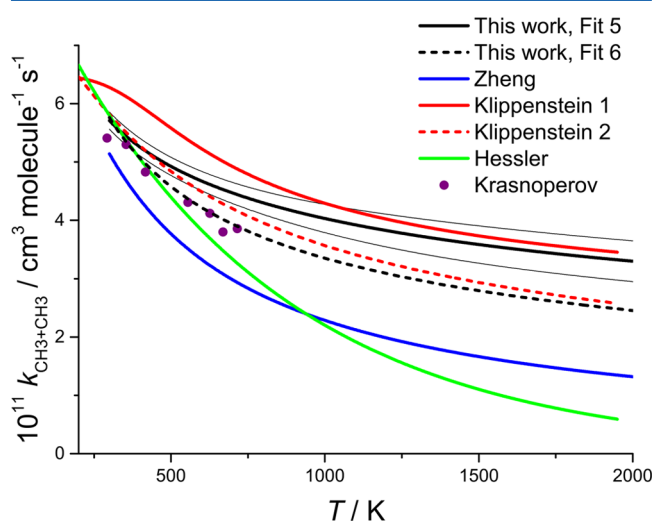


Figure 6. Temperature dependence of $k_{\infty}(T)$ for CH₃ + CH₃ showing the best fit results from fits 5 and 6 (Table 3) and the statistical uncertainty limits for fit 5; the narrow black lines show the upper and lower 2σ uncertainties from the analysis discussed in Section 4.3. The theoretical results from Klippenstein 1¹¹ and Klippenstein 2¹⁰ and Zheng et al.⁶¹ are also shown, together with the best fit results to experimental data from Hessler and Ogren¹⁵ and the recent results by Sangwan et al.⁶²

in section 5. The percentage uncertainties, at the 2σ level, increase from 3.1% at 300 K to 8.7% at 1500 K. They solely reflect the statistical errors from the fits and do not contain any contribution from the uncertainty in the cross section; the latter can be gauged from the fits using models I and II for the cross section, which are shown using fits 5 and 6 in Figure 6.

5. DISCUSSION

5.1. High Pressure Limit. $k_{\infty}(T)$ for CH₃ + CH₃ at temperatures up to 900 K is well-defined by the pulsed photolysis/absorption spectroscopy data of Slagle et al.,¹² and the *A* and *n* parameters are little changed in the fits that include data obtained at lower pressures. Inclusion of the shock tube data of Oehlschlaeger et al.¹⁹ increases the negative temperature dependence slightly, but the values of $k_{\infty}(2000 \text{ K})$ from the best fit parameters from fits 4 and 5 differ by only 3%, well within the fitting uncertainties discussed in the previous section. It should be noted that those uncertainties solely reflect the statistical errors from the fits and do not contain any contribution from the uncertainty in the cross section. The latter can be gauged from the parameters in Table 3 obtained using models I and II for the cross section (fits 5 and 6) and the plots of $k_{\infty}(T)$ shown in Figure 6. The best fit values for fit 6 differ from those for fit 5 by 0.8% at 300 K and 24% at 2000 K. The overall uncertainty in $k_{\infty}(T)$, at the 2σ level, is thus $\sim \pm 10\%$ at 300 K and $\sim \pm 20\%$ at 2000 K, where the differences between the results from models I and II have been used to estimate the likely uncertainties in the cross sections. The absolute values of the cross sections were fixed mainly by reference to the experimental data of Macpherson et al.,¹³ which were quoted with errors of $\pm 5\%$, which are included in

these final uncertainties. The comparison between the calculated cross sections and the experimental values of Oehlschlaeger et al.¹⁶ was used to test the cross section model at high temperatures and demonstrated the need to include a vibrational background contribution to the values determined from models I and II. This vibrational background was insignificant at temperatures up to 900 K, the range needed for the cross section corrections used in the redetermination of the rate coefficients from Slagle et al.¹²

Though model II + vibrational background provided the best fit to the experimental high temperature cross sections, the master equation fits to the rate data were somewhat better with model I for the low T correction. It is difficult, therefore, to distinguish between the results from models I and II. The most appropriate representation is the mean of the two giving $k_{\infty}(T) = 5.76 \times 10^{-11}(T/298 \text{ K})^{-0.34} \text{ cm}^3 \text{ molecule}^{-1} \text{ s}^{-1}$.

The most detailed predictive calculations of $k_{\infty}(T)$ for $\text{CH}_3 + \text{CH}_3$ were performed by Klippenstein et al.¹⁰ They used variational reaction coordinate transition state theory with a corrected CASPT2/cc-pvdz potential energy surface. They applied a 15% reduction in the rate coefficient to correct for local recrossings of the transition state dividing surface, deduced from dynamical calculations. They obtained $k_{\infty}(T) = 1.57 \times 10^{-9} T^{-0.538} \exp(-68 \text{ K}/T)$. As shown in Figure 6, this expression shows a steeper temperature dependence than obtained from model I but is comparable to the results from model II. The agreement is good at 300 K and differs at 2000 K by 27% for fit 5 and only 4% for fit 6; the difference for the mean value expression quoted above is 16%. This is very satisfactory agreement given the long extrapolation in p and T involved. Figure 6 also shows the calculated results obtained by Klippenstein and Harding¹¹ in an earlier analysis based on an MRCI potential, without a dynamical correction. A further plot is shown of the data of Zheng et al.,⁶¹ who used density functional theory (M06-L), obtaining a stronger negative T dependence. Figure 6 also shows the results from Hessler and Ogren,¹⁵ based on fitting experimental data to a number of analytic representations of $k(p,T)$. They recommended $k_{\infty}(T) = 8.78 \times 10^{-11} \exp(-T/723 \text{ K})$, which shows a stronger negative temperature dependence than the present analysis. In a later paper, Hessler⁶³ showed that the data are compatible with a range of T dependences, including one close to that found here, depending on the fitting method used.

Sangwan et al.⁶² have recently determined $k_{\infty}(T)$ for $\text{CH}_3 + \text{CH}_3$ using high pressure pulsed photolysis, coupled with absorption spectroscopy. Their results are shown in Figure 6 and agree well with those obtained here, lying close to the results from model II.

Other analyses of experimental data and application of theoretical models to obtain $k_{\infty}(T)$ have recently been discussed by Pilling.⁶⁴ Cobos and Troe⁶⁵ used a simplified two-parameter version of the statistical adiabatic channel model, tuning one of the parameters to the then available experimental data and obtaining $k_{\infty}(300 \text{ K}) = 4.7 \times 10^{-11} \text{ cm}^3 \text{ molecule}^{-1} \text{ s}^{-1}$ and $k_{\infty}(1300 \text{ K}) = 5.4 \times 10^{-11} \text{ cm}^3 \text{ molecule}^{-1} \text{ s}^{-1}$. Wagner and Wardlaw⁶⁶ used a microcanonical RRKM model, based on flexible transition state theory, coupled with a weak collision, integral representation of falloff, to fit the data of Slagle et al., obtaining $k_{\infty}(T) = 1.50 \times 10^{-7} T^{-1.18} \exp(-329 \text{ K}/T) \text{ cm}^3 \text{ molecule}^{-1} \text{ s}^{-1}$. Baulch et al.⁴ evaluated the available experimental data in 2005 recommending a temperature invariant high pressure limit of $6.0 \times 10^{-11} \text{ cm}^3 \text{ molecule}^{-1} \text{ s}^{-1}$, but with an uncertainty of a factor of 2. Wang et al.⁵⁴

calculated $k_{\infty}(T)$ using flexible transition state theory, based on an *ab initio* potential, fitting with a master equation model to available experimental data, including their own, to determine energy transfer parameters. They calculated $k_{\infty}(T) = 7.42 \times 10^{-11}(T/298 \text{ K})^{-0.69} \exp(-88 \text{ K}/T) \text{ cm}^3 \text{ molecule}^{-1} \text{ s}^{-1}$.

5.2. Low Pressure Limit. The low pressure limiting rate coefficient, $k_0(T)$, was determined from the master equation, with the best fit parameters for fits 5 and 6, with Ar as bath gas, by successively decreasing the bath gas concentration until $k(p,T)$ varied linearly with pressure at a given temperature. The resulting values are given in the Supporting Information, together with the values recommended in the evaluation of Baulch et al.,⁴ which were determined using Troe fits⁶ to the then available data. The agreement is to within a factor of ~ 8 at 300 K falling to 0.3 at 1500 K (ratio of values from this work to those from Baulch et al.⁴). The results from fits 5 and 6 agree to within $\sim 30\%$ at 300 K, decreasing to $<10\%$ at 1500 K. The best fit mean parametrization is $k_0(T) = 1.48 \times 10^{-22}(T/298)^{-10.04} \exp(-2209 \text{ K}/T) \text{ cm}^6 \text{ molecule}^{-2} \text{ s}^{-1}$.

5.3. Energy Transfer Parameters. The energy transfer parameters in the low temperature regime ($<1000 \text{ K}$) are reasonably well-defined for Ar and He. Jasper et al.⁵⁸ recently calculated $\langle \Delta E \rangle_{\text{down}}$ from first-principles using classical trajectories on potential energy surfaces obtained by simple (tight binding + $\exp/6$ attraction) representations that were thoroughly tested for $\text{CH}_4 + \text{He}$, Ne and H_2 , and $\text{C}_2\text{H}_6 + \text{He}$ collisions against direct dynamics calculations. Their values for $\text{C}_2\text{H}_6/\text{Ar}$ range from 185 to 390 cm^{-1} over the temperature range 300–900 K, compared with the values from the present analysis of 279–555 cm^{-1} (model I, fit 4); the difference is $\sim 40\%$ throughout the temperature range. The 1σ experimental uncertainties in $\langle \Delta E \rangle_{\text{down,ref}}$ and m are 10% and 16%, respectively. The differences in the temperature dependence are somewhat larger for He, but the values themselves are closer, with the calculated values ranging from 168–359 cm^{-1} and the experimental values from 103–387 cm^{-1} over the more restricted temperature range 300–700 K. The experimental uncertainties in $\langle \Delta E \rangle_{\text{down,ref}}$ and m for He are 14% and 12% respectively.

The agreement for Ar at higher temperatures is less good. Extrapolating the energy transfer parameters from fit 4 to temperatures above 1000 K shows improved agreement with the values obtained by Jasper et al.,⁶⁷ with only a 20% difference at 2000 K. However, these values fit the data of Oehlschlaeger et al.¹⁹ poorly. Three approaches were applied. In the first, a three-parameter fit was used for $\langle \Delta E \rangle_{\text{down}}$ as discussed in section 4. This results in a maximum in $\langle \Delta E \rangle_{\text{down}}$ at $\sim 1300 \text{ K}$ of $\sim 600 \text{ cm}^{-1}$, followed by a slow decrease to $\sim 500 \text{ cm}^{-1}$ at 2000 K; Jasper et al. obtained $\langle \Delta E \rangle_{\text{down}} = 444 \text{ cm}^{-1}$ at 1000 K and 789 cm^{-1} at 2000 K. Alternatively, as discussed in the Supporting Information, we used separate fits for $\langle \Delta E \rangle_{\text{down}}$ below and above 1000 K, constraining the ILT A and n parameters to the same values across the temperature range. This resulted in high temperature values for $\langle \Delta E \rangle_{\text{down,ref}}$ and m of 677 cm^{-1} and -0.09 , respectively, for $T_{\text{ref}} = 1400 \text{ K}$, corresponding to values of $\langle \Delta E \rangle_{\text{down}}$ of 686 cm^{-1} at 1200 K and 655 cm^{-1} at 2000 K, respectively. Finally, attempts were made to use a three-parameter representation of $k_{\infty}(T) (=A(T/300 \text{ K})^n \exp(-C/T))$, which would allow a more flexible representation of $k(E)$. The ILT technique, as implemented in MESMER, does not permit a negative activation energy which would require nonzero values of $k(E)$ below the dissociation threshold. Minimizing χ^2 forced C toward zero

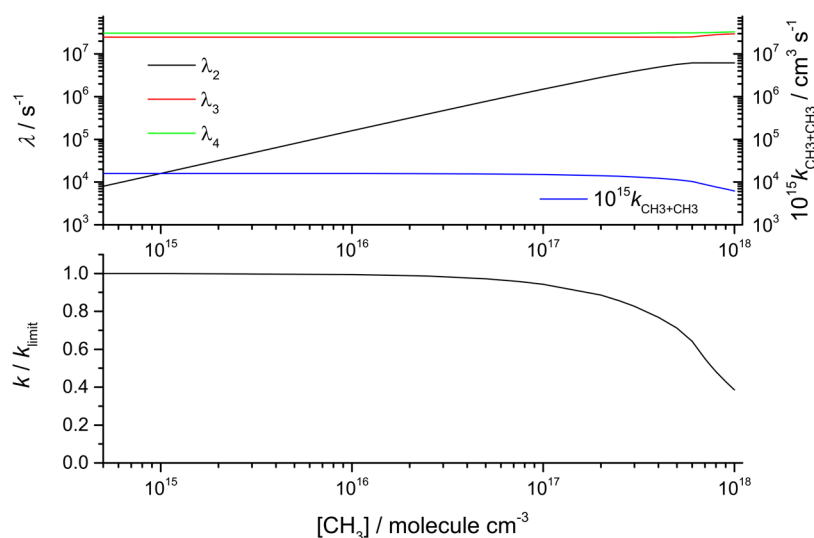


Figure 7. (a) Nonzero chemically significant eigenvalue, λ_2 , and the two internal energy relaxation eigenvalues of smallest magnitude, λ_3 and λ_4 , as a function of $[\text{CH}_3]_a$, for $T = 900$ K and a total bath gas concentration of 10^{18} cm^{-3} . The rate coefficient for association, calculated from λ_2 , is also shown; under these conditions, $k_{\text{CH}_3+\text{CH}_3} = 1.60 \times 10^{-11} \text{ cm}^3 \text{ molecule}^{-1} \text{ s}^{-1} = k_{\text{limit}}$. (b) Plot of $k_r/k_{r,\text{limit}}$ vs $[\text{CH}_3]$ for $T = 900$ K and a total bath gas concentration of 10^{18} cm^{-3} . $k_{r,\text{limit}}$ is the limiting value as $[\text{CH}_3]_a$ tends to zero (see Figure 7a and its caption); the plot shows the convergence of the rate coefficient under the conditions used in the data fitting, where $[\text{CH}_3]_a = 10^{14} - 10^{15} \text{ cm}^{-3}$ was used. The slight positive curvature at the highest $[\text{CH}_3]$ is a result of the eigenvalue mixing shown in Figure 7a by the onset of nonlinearity in λ_2 .

with no improvement in the fit over that found with two parameters. A three-parameter fit for $\langle \Delta E \rangle_{\text{down}}$ or the use of different parameters at high and low temperatures, were still necessary to obtain good fits across the whole temperature range.

The Supporting Information provides data on the energy transfer parameters for Kr, obtained from the experimental results of Yang et al.⁵⁶ These were parametrized for a reference temperature of 1500 K, in the middle of the experimental range. The values obtained were $\langle \Delta E \rangle_{\text{down,ref}} = 331 \text{ cm}^{-1}$ and $m = 0.40$, corresponding to $\langle \Delta E \rangle_{\text{down}}$ values of 234 cm^{-1} at 630 K and 386 cm^{-1} at 2200 K, the limits of the experimental temperature range.

The experimental range covered in the present analysis of the Ar data is wider than has previously been attempted in any direct fitting of a master equation model to experimental rate measurements. It is interesting that it was not possible to obtain a unique set of energy transfer parameters across the whole range. Golden⁷³ observed similar behavior fitting the experimental measurements of Slagle et al.¹² and of Oehlschlaeger et al.¹⁹ to a master equation with a Gorin model for the microcanonical dissociation rate constants, based on the high pressure limit of Klippenstein et al.¹⁰ (See Supporting Information I, section 3). This issue may be related to the recent application of calculated energy transfer parameters to master equation calculations of falloff in association reactions by Jasper et al.⁵⁸ They found that it was necessary to employ a 2-D master equation to incorporate collisional changes in both total energy and angular momentum in modeling the association reactions $\text{CH}_3 + \text{H}$ and $\text{C}_2\text{H}_3 + \text{H}$. Agreement with experiment in their fully *a priori* model was much improved when collisional changes in both E and J were allowed, compared with a 1-D model that allows only changes in E . The range of J values at high T is larger than that at low T , and the apparent deficiencies in the use of a 1-D model may explain the difficulties we encountered in the concomitant fitting of high and low temperature experimental data. It may

also explain the differences from the calculations of Jasper et al. The MESMER code currently cannot incorporate energy transfer parameters that depend on the total energy E . Such a facility is planned and will permit use of energy transfer parameters derived from trajectory calculations in fitting or comparing with experimental data.

5.4. Parametrization of the Rate Coefficient in the Falloff Region. Two methods were used to provide a parametric representation of the rate coefficient in the falloff region, by fitting the output of the master equation calculations. The first is based on Chebyshev polynomials. Rate coefficients in Chebyshev form⁷ can be used in CHEMKIN⁶⁸ and in CANTERA⁶⁹ simulations. A spreadsheet is provided (Supporting Information II) to facilitate routine use of the parameters to determine $k(p, T)$. The second method used was that recently discussed by Troe and Ushakov⁷⁰ which uses a modified broadening term, suitable for dissociation and association reactions. The forms of the parametrizations, together with the parameters, are given in the Supporting Information.

Because of the large number of parameters used, the Chebyshev parametrization reproduces the master equation more closely (within 1–2% across the fitted range) and can be used as an accurate representation of the master equation output. The Troe fits are also very satisfactory but, because they use fewer parameters, albeit based on a model derived from master equation analyses, they show larger deviations (up to 30–40% at $[M] = 1 \times 10^{16} \text{ molecules cm}^{-3}$ falling to 2–6% at $[M] = 1 \times 10^{20} \text{ molecules cm}^{-3}$). The smaller number of parameters used in the Troe fits facilitates their widespread use in data evaluations and compilations. A figure showing the fits is included in Supporting Information I.

5.5. Breakdown of the Local Linearization of the Rate Equation at High $[\text{CH}_3]$. The master equation methodology used to fit the experimental data relies on the local linearization developed in section 3. As discussed in that section, because the reaction is reversible and both CH_3 and C_2H_6 are recognized in the ME analysis, there are two chemically significant

eigenvalues, λ_1 and λ_2 ; the former is zero and relates to mass balance. $\lambda_2 = -(k_f + 4k_r[\text{CH}_3]_a)$ and the two rate coefficients can be separated using the equilibrium constant.

There is a limitation imposed by the truncation of the Taylor series and it is that the equation of motion is only valid for very short intervals of time. The Jacobian, and therefore λ_2 , depend on the methyl concentration, which necessarily changes as the system evolves. Therefore, the expansion limited to linear terms will only be valid for that period of time for which the change in methyl radical concentration is very small, and this time period will vary depending on where the system is on the evolution trajectory. At the end of this period the Jacobian and therefore λ_2 need to be re-evaluated. As discussed above, the approach accounts for the reversibility of the process. The master equation analysis refers to an infinitesimally short period of time in which $[\text{CH}_3]$ is invariant. Note that even though the eigenvalue of smallest magnitude is changing as $[\text{CH}_3]$ changes, the second-order rate coefficient is invariant.

The application of the master equation to association/dissociation reactions, with particular reference to $\text{CH}_3 + \text{CH}_3$, has been discussed by Davis and Klippenstein.⁴⁸ They showed that problems arise, especially at high $[\text{CH}_3]$. These derive from a number of potential sources, but there is a specific problem when the time scale of the association process becomes comparable with the time scales of collisional relaxation in C_2H_6^* . Davis and Klippenstein provided a particularly clear analysis of this aspect of the problem by reference to the Lindemann model for association. Problems arising from the overlap of chemically significant eigenvalues (CSEs) with eigenvalues for internal energy relaxations (IEREs) are widely recognized in master equation analyses of multiple well systems.^{71,72} Eigenvalue overlap was investigated for $\text{CH}_3 + \text{CH}_3$ to establish that such problems had been avoided in the data analysis. Figure 7 shows a plot, at 900 K and a bath gas concentration of 10^{18} molecule cm^{-3} , of λ_2 , λ_3 , and λ_4 vs $[\text{CH}_3]_a$; λ_3 and λ_4 are the two IEREs of smallest magnitude. Figure 7 also shows the rate coefficient, k_r , calculated from λ_2 ; k_f is negligible at 900 K.

At the lower values of $[\text{CH}_3]_a$, λ_2 increases linearly with $[\text{CH}_3]_a$ and k_r is constant. For $[\text{CH}_3]_a \gtrsim 5 \times 10^{16}$ molecule cm^{-3} , however, λ_2 increases more slowly with $[\text{CH}_3]_a$, there is a clear mixing between the three eigenvalues λ_2 – λ_4 and the apparent k_r decreases. These changes reflect those discussed in more detail by Davis and Klippenstein.⁴⁸ The deviation from linearity in λ_2 , and the decrease in k_r , occur for a greater separation of the CSEs and IEREs than is generally found in studies of linear multiwell reactions, reflecting the complexity in the dynamical behavior, as discussed by Davis and Klippenstein. Because the IEREs scale linearly with the bath gas concentration, the values for $[\text{CH}_3]_a$ at which the apparent rate coefficient begins to diverge from the true value increases with bath gas concentration. Figure 7b shows a plot of $k_r/k_{r,\text{limit}}$ vs $[\text{CH}_3]$, where $k_{r,\text{limit}}$ is the true value for the association rate coefficient, obtained at the limit low $[\text{CH}_3]$ where the dynamical complexities are eliminated. The plot was used to establish conditions under which accurate rate coefficients could be obtained: broadly speaking, the results are accurate provided $[\text{CH}_3]_a$ is at least a factor of 100 less than the bath gas concentration.

6. CONCLUSIONS

We have demonstrated the fitting of p and T dependent rate data for an association reaction using a master equation analysis

in which the microcanonical dissociation rate constants, $k_d(E)$, are linked to the high pressure limiting rate coefficient for association, $k_\infty(T)$, via inverse Laplace transformation (ILT). The fits have been made over an unprecedentedly wide range of temperature, so that the ILT parameters, A and n , are well-defined and compare well with the most accurate theoretical values. The final parameters obtained were primarily influenced by the absorption spectroscopy data obtained below 1000 K, which lie closest to the high pressure limit.

Jasper et al.⁵⁸ argued that it is necessary to use a 2D master equation, allowing collisional changes in both E and J , to accurately predict falloff behavior in association reactions. The use of the present fitting methodology is not compatible with such an approach, because the ILT procedure generates only $k_d(E)$ not $k_d(E,J)$, although it does contain the correct averaging over J in the high pressure limit; in addition, the large number of ME calculations needed in a data-fitting procedure are not currently feasible when a 2-D master equation model is used. An investigation of the relationship between energy transfer parameters obtained in 1-D and in 2-D ME models would be of value, especially in relation to the use of experimental data to obtain representations of rate coefficients for use in complex kinetic models.

The recommended expression for $k_\infty(T)$ is $5.76 \times 10^{-11}(T/298 \text{ K})^{-0.34} \text{ cm}^3 \text{ molecule}^{-1} \text{ s}^{-1}$ with an uncertainty of $\pm 10\%$ at 300 K increasing to $\pm 20\%$ at 2000 K. Chebyshev polynomials for calculating the rate coefficient as a function of pressure and temperature in Ar and He are given in the Supporting Information, together with a parametrization using the Troe and Ushakov procedure.⁷⁰

■ ASSOCIATED CONTENT

● Supporting Information

Three files of Supporting Information are available: Supporting Information I contains

1. The log file from the PGOPHER fit to the available ground state data can be found in Supporting Information III. The file also gives the constants for all the states used in model I.
2. The correction factors used to correct the rate coefficients of Slagle et al. for the absorption coefficients calculated using absorption coefficients from models I and II.
3. The results of fitting the data used in fit 5, but with different energy transfer parameters above and below 1000 K. The energy transfer parameters obtained by Golden⁷³ are given, and compared with those obtained in this paper.
4. The results of fitting the data used in fit 5 plus the experimental data of Du et al.¹⁸
5. The results of fitting the data used in fit 5 plus the experimental data of Yang et al.⁵⁶
6. Calculated values for $k_0(T)$ using the data from fits 5 and 6, together with a comparison of the recommendation of Baulch et al.⁴ and parametrization of the temperature dependence. Broadening factors for calculating $k(p,T)$ using the method of Troe and Ushakov.⁷⁰
7. Chebyshev polynomials for calculating $k(p,T)$ for $\text{CH}_3 + \text{CH}_3$. A spreadsheet is provided as a separate Supporting Information file to facilitate use of the Chebyshev polynomials. The instructions for using the spreadsheet to calculate $k(p,T)$ under any conditions within the fitted

range are given in the spreadsheet in Supporting Information II.

8. The MESMER input file, which includes the molecular data used in the master equation calculations.

Supporting Information II is a spreadsheet which can be used to calculate $k(p,T)$ from the Chebyshev polynomials under any conditions within the fitted range. Instructions for use are contained in the spreadsheet. Supporting Information III is the PGOPHER log file. The Supporting Information is available free of charge on the ACS Publications website at DOI: 10.1021/acs.jpca.5b01002.

AUTHOR INFORMATION

Corresponding Author

*M. J. Pilling. E-mail: m.j.pilling@leeds.ac.uk. Tel: ++44 1943 608239.

Notes

The authors declare no competing financial interest.

ACKNOWLEDGMENTS

We are grateful to Ahren Jasper for providing the energy transfer parameters from ref⁶⁷ and Lev Krasnoperov for providing the high pressure limiting rate coefficients included in Figure 6 prior to publication. We are grateful to EPSRC for funding for RJS under grant EP/J010871/1.

REFERENCES

- (1) Robertson, S. H.; Seakins, P. W.; Pilling, M. J. Low-Temperature Combustion and Auto-Ignition. In *Comprehensive Chemical Kinetics*; Pilling, M. J., Ed.; Elsevier: Amsterdam, 1997; Vol. 35.
- (2) Huestis, D. L.; Bougher, S. W.; Fox, J. L.; Galand, M.; Johnson, R. E.; Moses, J. I.; Pickering, J. C. Cross Sections and Reaction Rates for Comparative Planetary Aeronomy. *Space Sci. Rev.* **2008**, 139, 63–105.
- (3) Blitz, M. A.; Seakins, P. W. Laboratory Studies of Photochemistry and Gas Phase Radical Reaction Kinetics Relevant to Planetary Atmospheres. *Chem. Soc. Rev.* **2012**, 41, 6318–6347.
- (4) Baulch, D. L.; Bowman, C. T.; Cobos, C. J.; Cox, R. A.; Just, T.; Kerr, J. A.; Pilling, M. J.; Stocker, D.; Troe, J.; Tsang, W.; et al. Evaluated Kinetic Data for Combustion Modeling: Supplement II. *J. Phys. Chem. Ref. Data* **2005**, 34, 757–1397.
- (5) Troe, J. Theory of Thermal Unimolecular Reactions in the Fall-Off Range 1. Strong Collision Rate Constants. *Ber. Bunsen-Ges. Phys. Chem. Chem. Phys.* **1983**, 87, 161–169.
- (6) Gilbert, R. G.; Luther, K.; Troe, J. Theory of Thermal Unimolecular Reactions in the Fall-Off Range 2. Weak Collision Rate Constants. *Ber. Bunsen-Ges. Phys. Chem. Chem. Phys.* **1983**, 87, 169–177.
- (7) Naik, C.; Carstensen, H. H.; Dean, A. M. *Reaction Rate Representation Using Chebyshev Polynomials*. In Spring Meeting of the Combustion Institute, San Diego, CA, 2002; http://chemeng.mines.edu/Groups/Amdean/Public_Html/Pub/Wsspaperfinal.pdf.
- (8) Wardlaw, D. M.; Marcus, R. A. RRKM Reaction-Rate Theory for Transition-States of Any Looseness. *Chem. Phys. Lett.* **1984**, 110, 230–234.
- (9) Quack, M.; Troe, J. Complex-Formation in Reactive and Inelastic-Scattering - Statistical Adiabatic Channel Model of Unimolecular Processes III. *Ber. Bunsen-Ges. Phys. Chem. Chem. Phys.* **1975**, 79, 170–183.
- (10) Klippenstein, S. J.; Georgievskii, Y.; Harding, L. B. Predictive Theory for the Combination Kinetics of Two Alkyl Radicals. *Phys. Chem. Chem. Phys.* **2006**, 8, 1133–1147.
- (11) Klippenstein, S. J.; Harding, L. B. A Direct Transition State Theory Based Study of Methyl Radical Recombination Kinetics. *J. Phys. Chem. A* **1999**, 103, 9388–9398.
- (12) Slagle, I. R.; Gutman, D.; Davies, J. W.; Pilling, M. J. Study of the Recombination Reaction $\text{CH}_3 + \text{CH}_3 \rightarrow \text{C}_2\text{H}_6$ Part 1. Experiment. *J. Phys. Chem.* **1988**, 92, 2455–2462.
- (13) Macpherson, M. T.; Pilling, M. J.; Smith, M. J. C. Determination of the Absorption Cross-Section for CH_3 at 216.36 nm and the Absolute Rate-Constant for Methyl Radical Recombination over the Temperature Range 296–577 K. *J. Phys. Chem.* **1985**, 89, 2268–2274.
- (14) Macpherson, M. T.; Pilling, M. J.; Smith, M. J. C. The Pressure and Temperature-Dependence of the Rate-Constant for Methyl Radical Recombination over the Temperature-Range 296–577-K. *Chem. Phys. Lett.* **1983**, 94, 430–433.
- (15) Hessler, J. P.; Ogren, P. J. Recombination of Methyl Radicals 2. Global Fits of the Rate Coefficient. *J. Phys. Chem.* **1996**, 100, 984–992.
- (16) Oehlschlaeger, M. A.; Davidson, D. F.; Hanson, R. K. High-Temperature UV Absorption of Methyl Radicals Behind Shock Waves. *J. Quant. Spectrosc. Radiat. Transfer* **2005**, 92, 393–402.
- (17) Glowacki, D. R.; Liang, C. H.; Morley, C.; Pilling, M. J.; Robertson, S. H. MESMER: An Open-Source Master Equation Solver for Multi-Energy Well Reactions. *J. Phys. Chem. A* **2012**, 116, 9545–9560.
- (18) Du, H.; Hessler, J. P.; Ogren, P. J. Recombination of Methyl Radicals 1. New Data between 1175 and 1750 K in the Falloff Region. *J. Phys. Chem.* **1996**, 100, 974–983.
- (19) Oehlschlaeger, M. A.; Davidson, D. F.; Hanson, R. K. High-Temperature Ethane and Propane Decomposition. *Proc. Combust. Inst.* **2005**, 30, 1119–1127.
- (20) Kawaguchi, K. High-Resolution Fourier Transform Infrared Spectra of the CH_3 ν_3 and CH_2D ν_4 Bands. *Can. J. Phys.* **2001**, 79, 449–459.
- (21) Amano, T.; Bernath, P. F.; Yamada, C.; Endo, Y.; Hirota, E. Difference Frequency Laser Spectroscopy of the ν_3 -Band of the CH_3 Radical. *J. Chem. Phys.* **1982**, 77, 5284–5287.
- (22) Triggs, N. E.; Zahedi, M.; Nibler, J. W.; Debarber, P.; Valentini, J. J. High-Resolution Study of the ν_1 Vibration of CH_3 by Coherent Raman Photofragment Spectroscopy. *J. Chem. Phys.* **1992**, 96, 1822–1831.
- (23) Kelly, P. B.; Westre, S. G. Resonance Raman-Spectroscopy of the Methyl Radical. *Chem. Phys. Lett.* **1988**, 151, 253–257.
- (24) Westre, S. G.; Liu, X.; Getty, J. D.; Kelly, P. B. A Force-Field Analysis of the Methyl Radical X^2A_2 State Stretching Potential Using the Local Mode-Coupled Morse Oscillator Model. *J. Chem. Phys.* **1991**, 95, 8793–8802.
- (25) Yamada, C.; Hirota, E.; Kawaguchi, K. Diode-Laser Study of the ν_2 Band of the Methyl Radical. *J. Chem. Phys.* **1981**, 75, 5256–5264.
- (26) Hermann, H. W.; Leone, S. R. Photofragment Infrared-Emission Spectroscopy - Vibrational Progression and Potential Parameters of the $\text{CH}_3(\nu_2)$ Umbrella Mode. *J. Chem. Phys.* **1982**, 76, 4759–4765.
- (27) Snelson, A. Infrared Matrix Isolation Spectrum of Methyl Radical Produced by Pyrolysis of Methyl Iodide and Dimethyl Mercury. *J. Phys. Chem.* **1970**, 74, 537.
- (28) Jacox, M. E. Matrix-Isolation Study of IR-Spectrum and Structure of CH_3 Free-Radical. *J. Mol. Spectrosc.* **1977**, 66, 272–287.
- (29) Hoshina, H.; Fushitani, M.; Momose, T. Infrared Spectroscopy of Rovibrational Transitions of Methyl Radicals (CH_3 , CD_3) in Solid Parahydrogen. *J. Mol. Spectrosc.* **2011**, 268, 164–172.
- (30) Cunha de Miranda, B. K.; Alcaraz, C.; Elhanine, M.; Noller, B.; Hemberger, P.; Fischer, I.; Garcia, G. A.; Soldi-Lose, H.; Gans, B.; Mendes, L. A. V.; et al. Threshold Photoelectron Spectroscopy of the Methyl Radical Isotopomers, CH_3 , CH_2D , CHD_2 and CD_3 : Synergy between VUV Synchrotron Radiation Experiments and Explicitly Correlated Coupled Cluster Calculations. *J. Phys. Chem. A* **2010**, 114, 4818–4830.
- (31) Western, C. M. PGOPHER, a Program for Simulating Rotational Structure, Version 8.0; University of Bristol: Bristol, U.K., 2014; DOI 10.5523/Bris.Huflggvpcuc1zvliq497r2, URL <http://Pgopher.chm.bris.ac.uk>.
- (32) Meal, J. H.; Polo, S. R. Vibration-Rotation Interaction in Polyatomic Molecules 0.2. Determination of Coriolis Coupling Coefficients. *J. Chem. Phys.* **1956**, 24, 1126–1133.

- (33) Medvedev, D. M.; Harding, L. B.; Gray, S. K. Methyl Radical: Ab Initio Global Potential Surface, Vibrational Levels and Partition Function. *Mol. Phys.* **2006**, *104*, 73–81.
- (34) Herzberg, G. Bakerian Lecture - Spectra and Structures of Free Methyl and Free Methylene. *Proc. R. Soc. London, Ser. A* **1961**, *262*, 291.
- (35) Callear, A. B.; Metcalfe, M. P. Oscillator-Strengths of Bands of $B^2 A'_1-X^2 A''_2$ System of CD_3 and a Spectroscopic Measurement of Recombination Rate - Comparison with CH_3 . *Chem. Phys.* **1976**, *14*, 275–284.
- (36) Settersten, T. B.; Farrow, R. L.; Gray, J. A. Coherent Infrared-Ultraviolet Double-Resonance Spectroscopy of CH_3 . *Chem. Phys. Lett.* **2003**, *370*, 204–210.
- (37) Westre, S. G.; Kelly, P. B.; Zhang, Y. P.; Ziegler, L. D. Subpicosecond Predissociation Dynamics of the Methyl Radical Rydberg-3 S State. *J. Chem. Phys.* **1991**, *94*, 270–276.
- (38) Westre, S. G.; Gansberg, T. E.; Kelly, P. B.; Ziegler, L. D. Structure and Dynamics of Higher Vibronic Levels in the Methyl Radical Rydberg-3s State. *J. Phys. Chem.* **1992**, *96*, 3610–3615.
- (39) Botschwina, P.; Schick, E.; Horn, M. The Barrier to Dissociation in the $B^2 A'_1$ State of the Methyl Radical. *J. Chem. Phys.* **1993**, *98*, 9215–9217.
- (40) Mebel, A. M.; Lin, S. H. Excited Electronic States of the Methyl Radical. Ab Initio Molecular Orbital Study of Geometries, Excitation Energies and Vibronic Spectra. *Chem. Phys.* **1997**, *215*, 329–341.
- (41) Davidson, D. F.; Chang, A. Y.; Dirosa, M. D.; Hanson, R. K. A cw Laser-Absorption Diagnostic for Methyl Radicals. *J. Quant. Spectrosc. Radiat. Transfer* **1993**, *49*, 559–571.
- (42) Miller, J. A.; Klippenstein, S. J. Master Equation Methods in Gas Phase Chemical Kinetics. *J. Phys. Chem. A* **2006**, *110*, 10528–10544.
- (43) Pilling, M. J.; Robertson, S. H. Master Equation Models for Chemical Reactions of Importance in Combustion. *Annu. Rev. Phys. Chem.* **2003**, *54*, 245–275.
- (44) Klippenstein, S. J.; Miller, J. A. From the Time-Dependent, Multiple-Well Master Equation to Phenomenological Rate Coefficients. *J. Phys. Chem. A* **2002**, *106*, 9267–9277.
- (45) Barker, J. R. Multiple-Well, Multiple-Path Unimolecular Reaction Systems. I. Multiwell Computer Program Suite. *Int. J. Chem. Kinet.* **2001**, *33*, 232–245.
- (46) Robertson, S. H.; Pilling, M. J.; Baulch, D. L.; Green, N. J. B. Fitting of Pressure-Dependent Kinetic Rate Data by Master Equation Inverse Laplace Transform Analysis. *J. Phys. Chem.* **1995**, *99*, 13452–13460.
- (47) Georgievskii, Y.; Miller, J. A.; Burke, M. P.; Klippenstein, S. J. Reformulation and Solution of the Master Equation for Multiple-Well Chemical Reactions. *J. Phys. Chem. A* **2013**, *117*, 12146–12154.
- (48) Davis, M. J.; Klippenstein, S. J. Geometric Investigation of Association/Dissociation Kinetics with an Application to the Master Equation for $CH_3+CH_3 \rightleftharpoons C_2H_6$. *J. Phys. Chem. A* **2002**, *106*, 5860–5879.
- (49) Bartis, J. T.; Widom, B. Stochastic-Models of Interconversion of 3 or More Chemical Species. *J. Chem. Phys.* **1974**, *60*, 3474–3482.
- (50) Davies, J. W.; Green, N. J. B.; Pilling, M. J. The Testing of Models for Unimolecular Decomposition Via Inverse Laplace Transformation of Experimental Recombination Data. *Chem. Phys. Lett.* **1986**, *126*, 373.
- (51) Robertson, S. H.; Glowacki, D. R.; Liang, C.-H.; Morley, C. M.; Pilling, M. J. MESMER (Master Equation Solver for Multi-Energy Well Reactions); an Object Oriented C++ Programme for Carrying out Master Equation Calculations and Analysis on Arbitrary Multiple Well Systems, 2009; <http://sourceforge.net/projects/mesmer>.
- (52) Hippler, H.; Luther, K.; Ravishankara, A. R.; Troe, J. High-Pressure Effects in the Recombination Reaction $CH_3+CH_3 \rightarrow C_2H_6$. *Z. Phys. Chem.* **1984**, *142*, 1–12.
- (53) Pereira, R. D.; Baulch, D. L.; Pilling, M. J.; Robertson, S. H.; Zeng, G. Temperature and Pressure Dependence of the Multichannel Rate Coefficients for the CH_3+OH System. *J. Phys. Chem. A* **1997**, *101*, 9681–9693.
- (54) Wang, B. S.; Hou, H.; Yoder, L. M.; Muckerman, J. T.; Fockenberg, C. Experimental and Theoretical Investigations on the Methyl-Methyl Recombination Reaction. *J. Phys. Chem. A* **2003**, *107*, 11414–11426.
- (55) Glänzer, K.; Quack, M.; Troe, J. Spectroscopic Determination of Methyl Radical Recombination Rate Constant in Shock-Waves. *Chem. Phys. Lett.* **1976**, *39*, 304–309.
- (56) Yang, X. L.; Goldsmith, C. F.; Tranter, R. S. Decomposition and Vibrational Relaxation in CH_3I and Self-Reaction of CH_3 Radicals. *J. Phys. Chem. A* **2009**, *113*, 8307–8317.
- (57) Goos, E.; Burcat, A.; Ruscic, B. Extended Third Millennium Ideal Gas Thermochemical Database with Updates from Active Thermochemical Tables, 2014, <http://burcat.technion.ac.il/dir>.
- (58) Jasper, A. W.; Pelzer, K. M.; Miller, J. A.; Kamarchik, E.; Harding, L. B.; Klippenstein, S. J. Predictive a Priori Pressure-Dependent Kinetics. *Science* **2014**, *346*, 1212–1215.
- (59) Shannon, R. J.; Tomlin, A. S.; Robertson, S. H.; Blitz, M. A.; Pilling, M. J.; Seakins, P. W. Global Uncertainty Propagation and Sensitivity Analysis in the $CH_3OCH_2 + O_2$ System: Combining Experiment and Theory to Constrain Key Rate Coefficients in DME Combustion. *J. Phys. Chem. A* **2015**, DOI: 10.1021/acs.jpca.5b00620.
- (60) Kucherenko, S.; Tarantola, S.; Annoni, P. Estimation of Global Sensitivity Indices for Models with Dependent Variables. *Comput. Phys. Commun.* **2012**, *183*, 937–946.
- (61) Zheng, J. J.; Zhang, S. X.; Truhlar, D. G. Density Functional Study of Methyl Radical Association Kinetics. *J. Phys. Chem. A* **2008**, *112*, 11509–11513.
- (62) Sangwan, M.; Yan, C.; Chesnokov, E. N.; Krasnoperov, L. Reaction $CH_3 + CH_3 \rightarrow C_2H_6$ Studied over the 292–714 K Temperature and 1–100 Bar Pressure Ranges. *J. Phys. Chem. A* **2015**, DOI: 10.1021/jp5b01276.
- (63) Hessler, J. P. Global Fits of Methyl-Methyl Recombinational Data to Prezhdo's New Interpolation Formula. *J. Phys. Chem.* **1996**, *100*, 2141–2144.
- (64) Pilling, M. J. Reactions of Hydrocarbon Radicals and Biradicals. *J. Phys. Chem. A* **2013**, *117*, 3697–3717.
- (65) Cobos, C. J.; Troe, J. Theory of Thermal Unimolecular Reactions at High-Pressures 0.2. Analysis of Experimental Results. *J. Chem. Phys.* **1985**, *83*, 1010–1015.
- (66) Wagner, A. F.; Wardlaw, D. M. Study of the Recombination Reaction $CH_3+CH_3 \rightarrow C_2H_6$ 2. Theory. *J. Phys. Chem.* **1988**, *92*, 2462–2471.
- (67) Jasper, A. W.; Oana, C. M.; Miller, J. A. Third-Body Collision Efficiencies for Combustion Modeling: Hydrocarbons in Atomic and Diatomic Baths. *Proc. Combust. Inst.* **2015**, *35*, 197–204.
- (68) Kee, R. J.; Rupley, F. M.; Miller, J. A. *Chemkin Software Sand89–8003*; Sandia National Laboratory, 1989.
- (69) CANTERA. <http://Code.Google.Com/P/Cantera/>. 2015.
- (70) Troe, J.; Ushakov, V. G. Representation of “Broad” Falloff Curves for Dissociation and Recombination Reactions. *Z. Phys. Chem.* **2014**, *228*, 1–10.
- (71) Miller, J. A.; Klippenstein, S. J. Determining Phenomenological Rate Coefficients from a Time-Dependent, Multiple-Well Master Equation: “Species Reduction” at High Temperatures. *Phys. Chem. Chem. Phys.* **2013**, *15*, 4744–4753.
- (72) Robertson, S. H.; Pilling, M. J.; Jitariu, L. C.; Hillier, I. H. Master Equation Methods for Multiple Well Systems: Application to the 1-,2-Pentyl System. *Phys. Chem. Chem. Phys.* **2007**, *9*, 4085–4097.
- (73) Golden, D. M. What Do We Know About the Iconic System $CH_3+CH_3+M \rightleftharpoons C_2H_6+M$? *Z. Phys. Chem.* **2011**, *225*, 969–982.